
Title	Two-dimensional transition-metal dichalcogenides-based membrane for ultrafast solvent permeation
Author(s)	Edison Huixiang Ang and Jia Wei Chew
Source	<i>Chemistry of Materials</i> , 31(24), 1002-10007
Published by	American Chemical Society

Copyright © 2019 American Chemical Society

This is an Accepted Manuscript of an article published by American Chemical Society in *Chemistry of Materials* on 22/11/2019, available online:
<https://doi.org/10.1021/acs.chemmater.9b01873>

Notice: Changes introduced as a result of publishing processes such as copy-editing and formatting may not be reflected in this document. For a definitive version of this work, please refer to the published source.

Two-dimensional transition-metal dichalcogenides-based membrane for ultrafast solvent permeation

Edison Huixiang Ang^{a,b,**} and Jia Wei Chew^{a,c,*}

^aSchool of Chemical and Biomedical Engineering, Nanyang Technological University, Singapore 637459, Singapore.

^bNatural Sciences and Science Education, National Institute of Education, Nanyang Technological University, Singapore 637616, Singapore.

^cSingapore Membrane Technology Centre, Nanyang Environmental and Water Research Institute, Nanyang Technological University, Singapore 637141, Singapore

KEYWORDS: two-dimensional · metal-dichalcogenides · ultrafast · solvent · permeation

ABSTRACT: Transition metal dichalcogenides (TMDs) represent an emerging class of materials showing promise in a variety of applications. The judicious stacking of two-dimensional (2D) TMDs has been reported to give high-flux and energy-efficient membranes for high-resolution molecular sieving, with permeation greater than the state-of-the-art graphene-based membranes of comparable thickness. Unfortunately, current TMDs-based membranes can only be used for aqueous solution but not organic solvents, which limit their scope of application. Furthermore, it remains a challenge not only to reduce the spacing of interlayers sufficiently to exclude small molecules, but also to maintain the high resolution in the face of the expected swelling when immersed in organic solvents for prolonged periods. Herein, we demonstrate the precise control of the interlayer spacing of anionic TMDs laminates using cationic layered double hydroxide (LDH) nanosheets. Moreover, the controlled interlayer distance of the TMD/LDH lamellar (TLL) membrane exhibited almost 100% rejection of organic dyes with molecular weight as small as 327 g mol⁻¹ dissolved in acetone, while maintaining excellent long-term stability at an ultrafast permeance that is 2–3 orders-of-

26 magnitude higher than that of the reported ones with similar rejection. Our study opens up new
27 perspectives for the use of 2D TLL membranes in a variety of critical separation technologies.

28 **INTRODUCTION**

29 Membrane technology confers many advantages over the conventional thermal techniques such
30 as distillation or evaporation because of its simplicity, scalability and energy efficiency.^{1,2}
31 Unfortunately, the instability of many polymeric membranes in organic solvents limits their
32 practical application in the chemical and pharmaceutical industries. Therefore, the
33 development of novel inorganic membranes for organic solvent nanofiltration (OSN) has
34 become increasingly important.³ Together with other beneficial properties, such as excellent
35 chemical stability⁴ and self-cleaning ability,⁵ such inorganic membranes are becoming very
36 promising candidates thriving in diverse separation environments as well as exhibiting
37 sustainable low-maintenance features. 2D materials, particularly graphene and graphene oxide
38 (GO), have been extensively explored for nanofiltration because the membrane thickness can
39 be controlled well by customizing the suspension concentration during membrane fabrication.
40 These membranes provide versatility for adaptation to different applications, because the
41 solvent permeability and solute rejection can be tuned by altering the surface functionality.⁶
42 Also, they have demonstrated much higher solvent flux than commercial membranes with
43 similar rejection⁷. However, GO-based membranes are prone to swelling when exposed to
44 aqueous or organic solvents, which causes the separation performance to degrade with time.^{8,9}
45 It has been recently demonstrated that, by restricting the interlayer spacing of the GO laminae,
46 higher ionic rejection can be achieved but at the cost of lower water permeability.^{10,11} Recent
47 reports suggest that TMD materials, another promising layered 2D material, can also be
48 beneficial as a membrane for aqueous systems.^{12,13,14-16} As examples, MoS₂- and WS₂-based
49 membranes exhibited water permeance of 2 to 5 folds greater than that of the GO-based
50 membranes of comparable thickness.^{12,16} In addition, these TMD-based membranes displayed

51 excellent rejection of greater than 80%. Unfortunately, the rejection performance in organic
52 solvents have not been proven, which limits the scope of application. To bridge this gap, further
53 investigation to understand the nanofluidic phase behaviour of TMD-based membranes in
54 organic solvents is necessary. In this report, we explore the synergistic stacking effect of
55 anionic TMDs nanosheets, consisting of MS_2 ($M = Ni, Mo, \text{ and } W$), using cationic LDH
56 nanosheets, towards ultrafast organic solvent separation, and demonstrate its potential for OSN.

57

58 **MATERIALS AND METHODS**

59 **Preparation of TMD/LDH membranes.** The anionic 2D TMDs used in this study were NiS_2 ,
60 MoS_2 , and WS_2 nanosheets. The NiS_2 nanosheets were prepared based on our previously
61 reported wet-chemical method,¹⁷ while the MoS_2 and WS_2 nanosheets were prepared by solvent
62 exfoliation from their respective bulk materials.¹⁸ The cationic $NiAlLDH$ nanosheets were
63 prepared by a hydrothermal method based on urea hydrolysis followed by calcination under
64 nitrogen atmosphere and lastly exfoliated in formamide solvent.^{19,20} All the resultant
65 suspensions containing nanosheets were washed repeatedly until the pH value reached 7. The
66 TMDs membranes with different interlayer spacing were prepared by mixing the respective
67 anionic suspension with the cationic LDH suspension for 1 h, followed by vacuum-filtering the
68 mixture through a nylon ultrafiltration support (47 mm diameter Whatman filters with 200 nm
69 pore size). To obtain a uniform membrane, the suspension was diluted to 0.20 mg ml^{-1} and the
70 cationic LDH and anionic TMDs were mixed homogenously using a mechanical stirrer for 1
71 h, followed by vacuum-filtration on the nylon support in combination with stirring to prevent
72 the aggregation of the nanosheets. The membranes with different thicknesses were obtained by
73 filtering different volume of suspension through the nylon support. Notably, the influence by
74 the nylon support on selectivity and permeability was minimal due to the large pore size of the

75 support. After filtration, the membrane was soaked in the probe solvent at room temperature
76 for at least 24 h before performing the separation performance tests.

77 **Membrane characterizations.** TEM (JEOL-2100F with acceleration voltage of 200 kV) and
78 AFM (Bruker Multimode 8, operating using tapping mode) techniques were employed to
79 measure the lateral size of the TMDs and LDH nanosheets. The former technique was used to
80 confirm the existence of lamellar structure via elemental mapping, HR-TEM and SAED
81 pattern; and the latter technique was used to determine the thickness of individual nanosheets
82 and membrane thickness. The nanosheets of each kind were analysed to derive an average
83 lateral sizes of 1.6 μm and 1.2 μm and thicknesses of 3.6 nm and 0.5 nm for NiS₂ and NiAlLDH
84 nanosheets, respectively (see [Figure S1a-f](#)). To measure the thicknesses of the membranes, we
85 transferred the membrane from the alumina support to the silicon wafer by the fishing method²¹
86 and then performed the AFM measurements. The lamella was first dried in vacuum oven and
87 subsequently its interlayer distance was probed by XRD (Shimadzu thin film diffractometer
88 with Cu-K α irradiation of $\lambda = 1.5406 \text{ \AA}$). The elemental distribution of the hetero-membrane
89 was characterized by using the FESEM (JEOL-6700F SEM) equipped with energy-dispersive
90 EDX analyzer (Oxford Instruments, model 7426). The XPS survey and high-resolution
91 spectrum of O 1s core-level were analysed using an AXIS-Hsi, Kratos Analytical X-ray
92 photoelectron spectrometer with an excitation source of Al K $\alpha = 1486.71 \text{ eV}$. The mass ratio
93 of the TMD/LDH composite was verified using inductively coupled plasma optical emission
94 spectroscopy (ICPOES, Optima 8300 ICP-OES spectrometer, PerkinElmer) and carbon-
95 hydrogen-nitrogen-sulphur (CHNS, Vario Micro Cube) elemental analyser. The probing of
96 organic dye was measured using UV-Vis spectrometer (Shimadzu UV 2450) while the salt
97 concentration was measured using an ion conductivity meter (ECTESTER11+, Cole-Parmer).

98 **Evaluation of separation performances.** In a typical 2D membrane separation,⁸ the filtration
99 tests were performed using an air-pressurized filtration system with a feed capacity of 4 l

100 (Figure S6a). All the rejection and permeation tests were conducted at an operating pressure of
101 1 bar and at room temperature unless otherwise stated. To evaluate the molecular separation
102 performances of the membranes, we used MO, AF, and BB dyes; NaCl, MgCl₂, MgSO₄, and
103 Na₂SO₄ salts as probe solutes; while using acetone, acetonitrile, tetrahydrofuran, methanol,
104 toluene, heptane, dimethylformamide, water, ethanol, isopropanol, and 1-butanol as probe
105 solvents. The feed concentrations of dyes were 10 mg l⁻¹ and salts were 1 g l⁻¹. Notably, there
106 is negligible amount of rejection rate contributed by the nylon ultrafiltration support.²² All the
107 filtration tests were stirred at a rate of 500 r.p.m to minimize concentration polarization. In
108 addition, the concentrations of dyes were quantified using a UV-vis spectrophotometer and the
109 concentration of salts were quantified using an ion conductivity meter. Each membrane type
110 was fabricated using the same protocol at least three times and tested to ascertain
111 reproducibility. The variabilities are shown as error bars in the figures. The effective area for
112 filtration was estimated to be 1.3 cm². For photocatalytic anti-fouling tests, it was performed
113 using a modified vacuum filtration set-up (see Movie S1). First, pure acetone solvent was
114 filtered through the membrane followed by air-pressurized filtering BB/acetone solution
115 through the membrane, then subsequently, flushed with water under light illumination using a
116 solar simulator (300 W Xenon lamp, CEL-HXF300, Beijing CEL. Tech. Co., Ltd.), which
117 operated at a visible light source of 14 V and 16 A, and was positioned 15 cm above the photo-
118 assisted vacuum filtration module. Finally, pure acetone solvent was passed through the air-
119 pressurized filtration system after photo-assisted cleaning to derive the permeance recovery
120 percentage. The solute permeation measurements were carried out using the set-up shown in
121 Figure S15a, which consists of a feed solution and pure solvent compartments, both of which
122 were filled with equal volumes and stirred continuously throughout the measurements. The
123 concentrations of solute in the feed and permeate compartments were quantitatively measured
124 using UV-vis spectrometer and the solute permeation experiments at different temperatures

125 were conducted using a heater equipped with a temperature controller, so to ensure the solution
126 was maintained at a constant temperature during the measurements. The permeance was
127 calculated as $V/(A \times t \times \Delta P)$, where A is the effective area of the membrane, t is the filtration time,
128 ΔP is the pressure drop, and V is the filtrate volume. The rejection percentage was calculated
129 as $(C_F - C_P / C_F) \times 100\%$, where C_F is the feed concentration and C_P is the permeate
130 concentration.

131

132 **RESULTS**

133 **Fabrication of TMD/LDH lamellar membranes.**

134 To illustrate our membrane fabrication procedure, the NiS₂ and NiAILDH nanosheets were
135 used. We selected NiAILDH to construct the TMD/LDH lamellar (TLL) membranes because
136 Ni-based materials are known to be stable in harsh solvents.^{17,23} NiS₂ was prepared by using
137 the wet chemical method,¹⁷ while the NiAILDH nanosheet was synthesized based on urea
138 hydrolysis followed by thermal decomposition and solvent exfoliation.^{19,20} The zeta potentials
139 of the NiS₂ and NiAILDH in aqueous solutions were measured to be around -32 and +40 mV,
140 respectively, the opposite charges of which would lead to spontaneous electrostatic
141 heterostacking.

142 The NiS₂/NiAILDH lamellar was prepared by mechanically stirring the mixed components in
143 aqueous solution followed by vacuum filtration. The obtained NiS₂/NiAILDH composites were
144 characterized by the transmission electron microscopy (TEM), selected area electron
145 diffraction (SAED), X-ray diffraction (XRD) and atomic force microscope (AFM). The TEM
146 image (Figure 1a) shows that the NiS₂/NiAILDH composite was composed of sheet-like
147 structures. The high-resolution (HR) TEM image (Figure 1b) reveals the lamellar lattice
148 fringes, with the alternating stripes of different contrasts representing the heterostacking of
149 NiS₂ and NiAILDH nanosheets. The diffraction rings in the SAED pattern (Figure 1c) further

150 confirmed that both TMD and LDH nanosheets were assignable, implying the successful self-
151 assembly of the two-component nanosheets on the microscopic scale. The XRD patterns
152 further confirm the self-assembly of the NiS₂ and NiAILDH hybrid (Figure 1d), with a distinct
153 peak at around 9.7° and several characteristic peaks in the range of 27.5° to 61.8° attributed to
154 NiAILDH and NiS₂, respectively. It is worth noting that the NiS₂/NiAILDH exhibited a
155 diffraction peak at 10.2°, representing a d-spacing of ~0.87 nm. The repeating dimension is
156 expected to be the sum of single-layered NiS₂ nanosheets (~ 3.6 nm thick) and NiAILDH
157 nanosheets (~ 0.5 nm thick), as shown in Figure S1; while the total thickness (4.1 nm) was
158 close to quintuple of the observed d-value. Moreover, the presence of S and O core levels, and
159 notable shift in binding energy of O 1s peak as shown in the X-ray photoelectron spectroscopy
160 (XPS) spectra, as well as the elemental mapping of S and Al elements from the energy-
161 dispersive X-ray spectroscopy, further confirmed the successfully fabricated NiS₂/NiAILDH
162 lamellated hybrid (Section S2).

163

164 **Separation performances**

165 To further evaluate the permeance of the membranes, we have performed dead-end filtration
166 using organic solutes with different molecular weights, namely, methyl orange (MO, 327 g
167 mol⁻¹), acid fuchsin (AF, 586 g mol⁻¹) and brilliant blue G (BB, 858 g mol⁻¹) (see Section S3).
168 To probe the separation performances of the NiS₂, NiAILDH and NiS₂/NiAILDH membranes,
169 we first evaluated the acetone permeances (Figure 2a) and the rejection of MO (Figure 2b) as
170 a function of membrane thickness at 1 bar. Although the 2θ value for NiAILDH/NiS₂ was 0.5°
171 (i.e., 0.4 Å) smaller than that of NiAILDH (Figure 1d), such a small difference in interlayer
172 spacing of 0.4 Å enabled better rejection at a slight trade-off of solvent permeability. In general,
173 the permeances decreased and rejection increased with increasing membrane thickness. While
174 thicker membranes conferred greater mass transfer resistance that reduced permeance, the

175 stacking of multiple nanosheets improved the rejection of smaller molecular solutes. Notably,
176 even though both the NiS₂ and NiAILDH had thicker selective layers of 600 nm, the rejection
177 were still 3–4 folds lower than the heterostacked NiS₂/NiAILDH membrane that exhibited
178 almost 100% rejection at a thickness of 250 nm (Figure 2c). A slight enhancement in rejection
179 and slight reduction in permeance for NiS₂ relative to NiAILDH membranes are attributed to
180 the lower zeta potential magnitude of the NiS₂ nanosheets giving a smaller interlayer spacing.
181 The excellent rejection of the NiS₂/NiAILDH membrane can be attributed to the highly packed
182 lamellar nature, which also contributed to a thinner membrane that enhanced the permeance by
183 2–3 folds vis-à-vis the pristine NiS₂ and NiAILDH membranes. Also, the flux of the
184 NiS₂/NiAILDH membrane (Figure 2d) was found to be linearly proportional to the pressure
185 gradient (ΔP), indicating that the as-fabricated membrane was robust under the range of
186 pressures. Moreover, the linear relationship between permeance and the reciprocal of solution
187 viscosity ($1/\eta$) reveals that the NiS₂/NiAILDH membrane was highly permeable in a wide range
188 of organic solvents and also water (Figure 2e). In particular, acetone exhibited the highest
189 permeance of 2464 l m⁻² h⁻¹ bar⁻¹ while 1-butanol exhibited the lowest permeance of 326 l m⁻²
190 h⁻¹ bar⁻¹. To further evaluate the separation efficacy of the NiS₂/NiAILDH membrane, filtration
191 experiments involving the acetone solvent were performed using organic solutes of different
192 molecular weights (Figure 2f). Although there was a slight decrease in permeance by ~6–14%
193 as the molecular weight of the solute increased (which is usually the case for nanofiltration),²⁴
194 the dye rejection were still ~100%, making these membranes outstanding candidates for OSN.
195 The self-assembly of TMDs with LDH nanosheets can be extended to other anionic 2D TMDs,
196 such as MoS₂ (with a zeta potential of –34 mV) and WS₂ (with a zeta potential of –38 mV)
197 nanosheets. Based on mass balance (i.e., feed solute mass = retentate solute mass + permeate
198 solute mass) and adsorption $(V_F C_F - V_R C_R - V_P C_P) / V_F C_F \times 100\%$, where C_F , C_P and C_R are the
199 concentrations of the feed, permeate, and retentate solution respectively, and V_F , V_P , and V_R are

200 the feed, permeate and retentate volumes of 150, 120 and 30 mL, respectively) considerations,
201 the results derived from the UV-vis spectra (Figure S6c-e) indicate negligible adsorption,
202 which implies that most dye molecules were rejected rather than adsorbed in the membranes.
203 This can also be supported by the constant rejection performances of membranes after the
204 prolonged separation processes (Figure S7a). To ascertain the stability of the TLL membranes,
205 different solvents were filtered through the membranes (Section S4). The results indicate that
206 the membranes exhibited excellent rejection in different solvents without significant decay in
207 permeances (Figure S7a-b), while the XRD characterizations ascertained negligible swelling
208 of the TLL membranes after prolonged exposure to solvents (Figures S9a-f), which affirm the
209 excellent stability of the TLL composite as an OSN membrane. Comparing the OSN
210 performance of the TLL membranes with the state-of-the-art OSN membranes (see Section
211 S5), results indicate that the former displayed ultrafast permeance that is 2–3 orders of
212 magnitude higher than the existing advanced membranes with similar solute retention (Figure
213 S10). These capabilities prove that our TLL membrane is a promising candidate for OSN
214 technology.

215 To determine application to other practical usage, we proved that our TLL membranes can also
216 be used for water desalination (see Section S6). For the first time, we also demonstrated that
217 green energy (i.e., sunlight) can be used in combination with water to remove the persistent
218 organic foulants deposited on the OSN membrane via photocatalytic degradation. The TLL
219 membrane could recover up to 99% of permeance after photo-assisted cleaning (see Section
220 S7 and Movie S1).

221 **Insights of separation mechanisms**

222 To elucidate the mechanisms underlying the organic solvent permeation and molecular sieving
223 behavior of the NiS₂/NiAILDH membrane, we conducted two additional sets of experiments.
224 Firstly, we performed XRD analyses for the NiS₂/NiAILDH membrane with different mass

225 ratios of TMD:LDH (T:L). [Figure 3a](#) indicates that the interlayer distance (d) decreased from
226 8.7 Å to 8.0 Å as the T:L mass ratio decreased from 1:1 to 1:8, but increased to 8.3 Å as the
227 T:L ratio further decreased to 1:10. The non-monotonic relationship between the T:L mass ratio
228 and interlayer distance of the NiS₂/NiAILDH composite is tied to the resultant charge density,
229 which affects the affinity and thereby the distance between the oppositely charged nanosheets;
230 the charges for the T:L mass ratios of 1:1, 1:8 and 1:10 were -25 mV, 0 mV and +29 mV,
231 respectively, as described in [Section S8](#). The interlayer distance is directly related to the trade-
232 off between permeance and molecular selectivity. Specifically, the permeation rate decreased
233 and rejection increased as the interlayer distance (d) decreased from 8.7 to 8.0 Å ([Figure 3b](#)).
234 Notably, the rejection of MO was a significant 99.9% at the T:L mass ratio of 1:8 ($d = 8.0$ Å),
235 when the NiS₂/NiAILDH membrane had a neutral total charge ([Section S8](#)) and thus least
236 interlayer repulsion. This indicates that the interlayer distance was successfully reduced by
237 controlling the mass ratio of hetero-charged components. It is worth noting that the acetone
238 permeance for our NiS₂/NiAILDH membranes was 6 orders-of-magnitude higher than those
239 estimated from the standard Hagen-Poiseuille equation using no-slip boundary conditions
240 ([Section S9](#)). Compared with the reported 2D and polymeric membrane, all of our TLL
241 membranes had permeability of 3 orders-of-magnitude greater than that with similar
242 rejections.²⁵

243 Secondly, to gain insights into the mechanism of solute permeation through our membranes,
244 we invoked Fick's law of diffusion,²⁶ which states that

$$245 \quad J \times \Delta x = D \times \Delta C \quad (1)$$

246 where J is molar flux, Δx is membrane thickness, D is the diffusion coefficient of the
247 solute (typically, $\sim 10^{-9}$ – 10^{-10} m² s⁻¹, see [Section S10](#)) and ΔC is the concentration gradient
248 across the membrane. Accordingly, we carried out experiments to obtain the linear plot of J
249 against $1/\Delta x$, and then normalized the slope with respect to ΔC to get the experimental D

250 value. The diffusion coefficient (D) expectedly increased with interlayer distance (Figure
251 S16, Supporting Information) or temperature (Figure S17), and decreased with the molecular
252 weight of the solute (Figure S16). In general, the relationship between diffusion coefficient and
253 temperature for the solute penetration through membrane follows the classical Arrhenius law:¹¹

$$254 \quad D = A \exp\left(-\frac{E_a}{k_B T}\right) \quad (2)$$

255 where A is the pre-exponential factor and E_a is the activation energy for the diffusion process,
256 k_B is the Boltzmann constant, and T is the absolute temperature. It is demonstrated that, by
257 decreasing the interlayer distance of the NiS₂/NiAILDH membrane, the slope of the plot of
258 diffusion coefficient (D) versus $1/T$ increased (Figure S17b), which indicates an increased
259 activation energy (E_a). The minimum energy required for the MO solute to diffuse in bulk
260 acetone solvent was found to be 2.5 kJ mol⁻¹. When a NiS₂/NiAILDH membrane with an
261 interlayer distance of 8.7 Å was used, the activation energy required for the MO solute to
262 diffuse through the membrane increased to 3.6 kJ mol⁻¹. This is because, for a solute to diffuse
263 through the interlayer distance (largest was 8.7 Å) that was smaller than the solvated
264 dimensions of the solute (i.e., for MO, it is 11.9 × 14.6 Å; see Table S1), the solvent shell had
265 to be removed from the solute. The removal of the solvent shell from the solute is highly
266 endergonic and thereby elevated the energy of activation for diffusion through the selective
267 layer. For the interlayer distance at 8.0 Å, the energy barrier was about two-fold higher than
268 that of the interlayer distance of 8.3 and 8.7 Å. This indicates that the former with a higher
269 energy barrier of entry had a better ability to shield the solute from entering the interlayers, and
270 thus increased the rejection of MO in acetone by ~2–3 times compared to that with a larger
271 interlayer distance (see Figure 3b). For a larger molecule (i.e., BB, 858 g mol⁻¹), the energy
272 barrier for entering through the interlayer distance of 8.0 Å increased sharply to 37.0 kJ mol⁻¹,
273 indicating that it is more difficult to remove the highly organized solvent network from the

274 larger molecule (Figure 3c). Furthermore, to understand the underlying mechanism of solute
275 permeation through the NiS₂/NiAILDH membrane, we have conducted permeation rate and
276 rejection tests at various feed concentrations (see Section S12). As shown in Figure S19a, the
277 permeation rate increased linearly with feed concentration, indicating the presence of the
278 solution-diffusion mechanism; while the display in Figure S19b shows that the rejection
279 remained constant with increasing feed concentration, indicating size-exclusion was also at
280 play.

281

282 **CONCLUSION**

283 In summary, we demonstrated the possibility to fine-tune the interlayer distance of the TLL
284 selective layer (in the range below 9.0 Å) by electrostatic heteroassembly of anionic TMDs
285 nanosheets and cationic LDH nanosheets. In this regime, the decreasing interlayer distance
286 enhanced the rejection exponentially. The proposed model based on energy barrier for solute
287 permeation explains the mechanism underlying the high rejection of sub-micrometre-thick TLL
288 membranes for ultrafast OSN. In addition, the inorganic TLL membranes possessed superior
289 organic solvent resistibility and unique photo-assisted anti-fouling ability, all of which are
290 promising for OSN, which is needed for the recovery of valuable products in the
291 pharmaceutical and chemical industries. The current molecular-scale heteroassembly strategy
292 using oppositely charged nanosheets presents a possible way to fabricate inorganic 2D-based
293 membranes with controllable interlayer distance for other gas or liquid separation applications.

294

295 **ASSOCIATED CONTENT**

296 **Supporting Information**

297 The Supporting Information is available free of charge on the ACS Publications website at

298 DOI:

299 Synthesis details and characterization of NiS₂ and NiAlLDH nanosheets, characterization of
300 TLL lamellar , OSN measurements with OSN performances, water desalination and photo-
301 assisted cleaning, solvent and solute permeation. (PDF)

302

303 **AUTHOR INFORMATION**

304 **Corresponding Author**

305 *Email for J. W. C: jchew@ntu.edu.sg

306 **Email for E. H. A: edison.ang@nie.edu.sg

307 **ORCID**

308 Jia Wei Chew: 0000-0002-6603-1649

309 Edison Huixiang Ang: 0000-0002-7869-268X

310 **Notes**

311 The authors declare no competing financial interest

312

313 **ACKNOWLEDGMENTS**

314 This work was supported by the Singapore Ministry of Education Academic Research Funds
315 Tier 2 (MOE2014-T2-2-074; ARC16/15) and Tier 1 (MOE2015-T1-001-023; RG7/15), and
316 the GSK (GlaxoSmithKline) – EDB (Economic Development Board) Trust Fund. We thank
317 C.W.H. Bobby for designing and fabricating the filtration units.

318

319 **REFERENCES**

320 (1) Lively, R. P.; Sholl, D. S. From water to organics in membrane separations. *Nat. Mater.*
321 2017, 16, 276.

322 (2) Hennessy, J.; Livingston Baker, A. membranes from academia to industry. *Nat. Mater.*
323 2017, 16, 280.

- 324 (3) Blumenschein, S.; Böcking, A.; Kätzel, U.; Postel, S.; Wessling, M. Rejection modeling
325 of ceramic membranes in organic solvent nanofiltration. *J. Membr. Sci.* 2016, *510*, 191-200.
- 326 (4) Szekely, G.; Jimenez-Solomon, M. F.; Marchetti, P.; Kim, J. F.; Livingston, A. G.
327 Sustainability assessment of organic solvent nanofiltration: from fabrication to application.
328 *Green Chem.* 2014, *16*, 4440-4473.
- 329 (5) Pan, J. H.; Zhang, X.; Du, A. J.; Sun, D. D.; Leckie, J. O. Self-etching reconstruction
330 of hierarchically mesoporous F-TiO₂ hollow microspherical photocatalyst for concurrent
331 membrane water purifications. *J. Am. Chem. Soc.* 2008, *130*, 11256-11257.
- 332 (6) Cheng, C.; Jiang, G.; Garvey, C. J.; Wang, Y.; Simon, G. P.; Liu, J. Z.; Li, D. Ion
333 transport in complex layered graphene-based membranes with tuneable interlayer spacing. *Sci.*
334 *Adv.* 2016, *2*, doi:10.1126/sciadv.1501272.
- 335 (7) Joshi, R. K.; Carbone, P.; Wang, F. C.; Kravets, V. G.; Su, Y.; Grigorieva, I. V.; Wu, H.
336 A.; Geim, A. K.; Nair, R. R. Precise and ultrafast molecular sieving through graphene oxide
337 membranes. *Science* 2014, *343*, 752-754.
- 338 (8) Yang, Q.; Su, Y.; Chi, C.; Cherian, C. T.; Huang, K.; Kravets, V. G.; Wang, F. C.; Zhang,
339 J. C.; Pratt, A.; Grigorenko, A. N.; Guinea, F.; Geim, A. K.; Nair, R. R. Ultrathin graphene-
340 based membrane with precise molecular sieving and ultrafast solvent permeation. *Nat. Mater.*
341 2017, *16*, 1198-1202.
- 342 (9) Yeh, C.-N.; Raidongia, K.; Shao, J.; Yang, Q.-H.; Huang, J. On the origin of the stability
343 of graphene oxide membranes in water. *Nat. Chem.* 2015, *7*, 166.
- 344 (10) Chen, L.; Shi, G.; Shen, J.; Peng, B.; Zhang, B.; Wang, Y.; Bian, F.; Wang, J.; Li, D.;
345 Qian, Z.; Xu, G.; Liu, G.; Zeng, J.; Zhang, L.; Yang, Y.; Zhou, G.; Wu, M.; Jin, W.; Li, J.; Fang,
346 H. Ion sieving in graphene oxide membranes via cationic control of interlayer spacing. *Nature*
347 2017, *550*, 380.

- 348 (11) Abraham, J.; Vasu, K. S.; Williams, C. D.; Gopinadhan, K.; Su, Y.; Cherian, C. T.; Dix,
349 J.; Prestat, E.; Haigh, S. J.; Grigorieva, I. V.; Carbone, P.; Geim, A. K.; Nair, R. R. Tunable
350 sieving of ions using graphene oxide membranes. *Nat. Nanotechnol.* 2017, *12*, 546.
- 351 (12) Sun, L.; Ying, Y.; Huang, H.; Song, Z.; Mao, Y.; Xu, Z.; Peng, X. Ultrafast molecule
352 separation through layered WS₂ nanosheet membranes. *ACS Nano* 2014, *8*, 6304-6311.
- 353 (13) Hirunpinyopas, W.; Prestat, E.; Worrall, S. D.; Haigh, S. J.; Dryfe, R. A. W.; Bissett, M.
354 A. Desalination and nanofiltration through functionalized laminar MoS₂ membranes. *ACS*
355 *Nano* 2017, *11*, 11082-11090.
- 356 (14) Deng, M.; Kwac, K.; Li, M.; Jung, Y.; Park, H. G. Stability, molecular sieving, and ion
357 diffusion selectivity of a lamellar membrane from two-dimensional molybdenum disulfide.
358 *Nano Lett.* 2017, *17*, 2342-2348.
- 359 (15) Heiranian, M.; Farimani, A. B.; Aluru, N. R. Water desalination with a single-layer
360 MoS₂ nanopore. *Nat. Commun.* 2015, *6*, 8616.
- 361 (16) Sun, L.; Huang, H.; Peng, X. Laminar MoS₂ membranes for molecule separation.
362 *Chem. Commun.* 2013, *49*, 10718-10720.
- 363 (17) Ang, H.; Hong, L. Engineering defects into nickel-based nanosheets for enhanced water
364 permeability. *J. Mater. Chem. A.* 2017, *5*, 20598-20602.
- 365 (18) Coleman, J. N.; Lotya, M.; O'Neill, A.; Bergin, S. D.; King, P. J.; Khan, U.; Young, K.;
366 Gaucher, A.; De, S.; Smith, R. J.; Shvets, I. V.; Arora, S. K.; Stanton, G.; Kim, H.-Y.; Lee, K.;
367 Kim, G. T.; Duesberg, G. S.; Hallam, T.; Boland, J. J.; Wang, J. J.; Donegan, J. F.; Grunlan, J.
368 C.; Moriarty, G.; Shmeliov, A.; Nicholls, R. J.; Perkins, J. M.; Grievson, E. M.; Theuwissen,
369 K.; McComb, D. W.; Nellist, P. D.; Nicolosi, V. Two-dimensional nanosheets produced by
370 liquid exfoliation of layered materials. *Science* 2011, *331*, 568-571.
- 371 (19) Ping, J.; Wang, Y.; Lu, Q.; Chen, B.; Chen, J.; Huang, Y.; Ma, Q.; Tan, C.; Yang, J.;
372 Cao, X.; Wang, Z.; Wu, J.; Ying, Y.; Zhang, H. Self-assembly of single-layer CoAl-layered

373 double hydroxide nanosheets on 3D graphene network used as highly efficient electrocatalyst
374 for oxygen evolution reaction. *Adv. Mater.* 2016, 28, 7640-7645.

375 (20) Constantino, V. R. L.; Thomas, J. P. Basic properties of $Mg^{2+}_{1-x}Al^{3+}_x$ layered double
376 hydroxide intercalated by carbonate, hydroxide, chloride, and sulfate anions. *Inorg Chem.*
377 1995, 34, 883-892.

378 (21) Karan, S.; Jiang, Z.; Livingston, A. G. Sub-10 nm polyamide nanofilms with ultrafast
379 solvent transport for molecular separation. *Science* 2015, 348, 1347-1351.

380 (22) Ang, H.; Hong, L. Polycationic Polymer-Regulated Assembling of 2D MOF
381 Nanosheets for High-Performance Nanofiltration. *ACS Appl. Mater. Interfaces* 2017, 9,
382 28079–28088

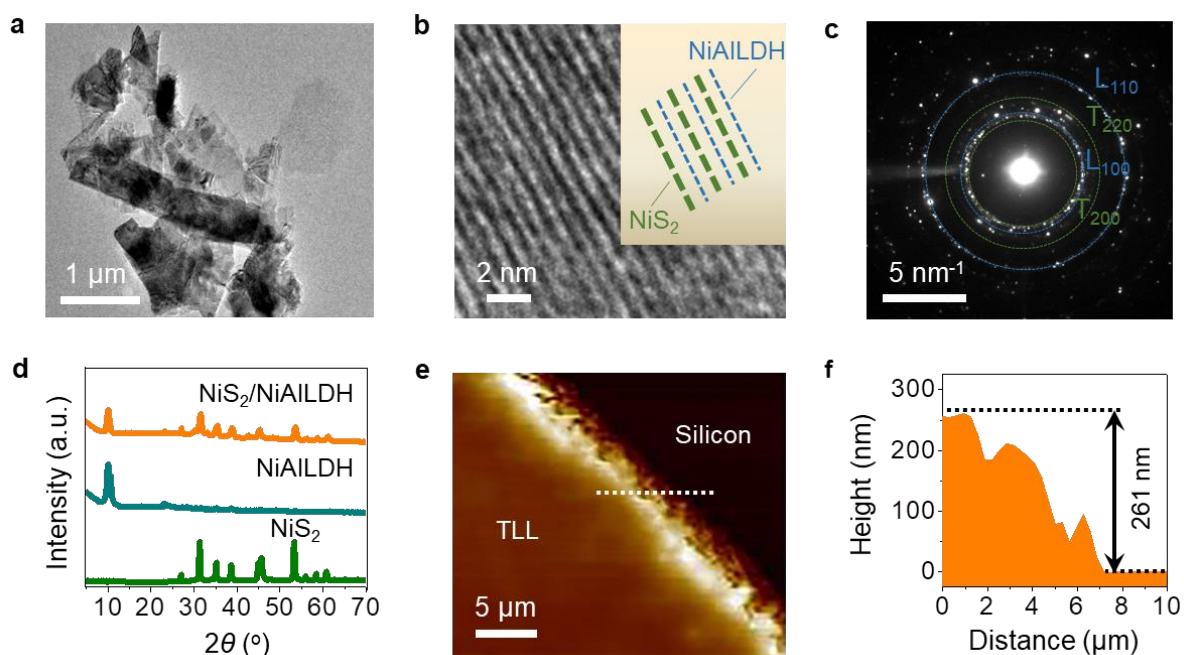
383 (23) Qu, Y.; Zhang, Q. G.; Soyekwo, F.; Gao, R. S. R.; Lv, X.; Lin, C. X.; Chen, M. M.; Zhu,
384 A. M.; Liu, Q. L. Nickel hydroxide nanosheet membranes with fast water and organics
385 transport for molecular separation. *Nanoscale* 2016, 8, 18428-18435.

386 (24) Han, Y.; Xu, Z.; Gao, C. Ultrathin graphene nanofiltration membrane for water
387 purification. *Adv. Funct. Mater.* 2013, 23, 3693-3700.

388 (25) Solomon, M. F. J.; Bhole, Y.; Livingston, A. G. High flux membranes for organic
389 solvent nanofiltration (OSN)—Interfacial polymerization with solvent activation. *J. Membr.*
390 *Sci.* 2012, 423-424, 371-382.

391 (26) Schreiber, L.; Schönherr, Jörg. Water and solute permeability of plant cuticles. first edn,
392 (Springer-Verlag Berlin Heidelberg, 2009).

393

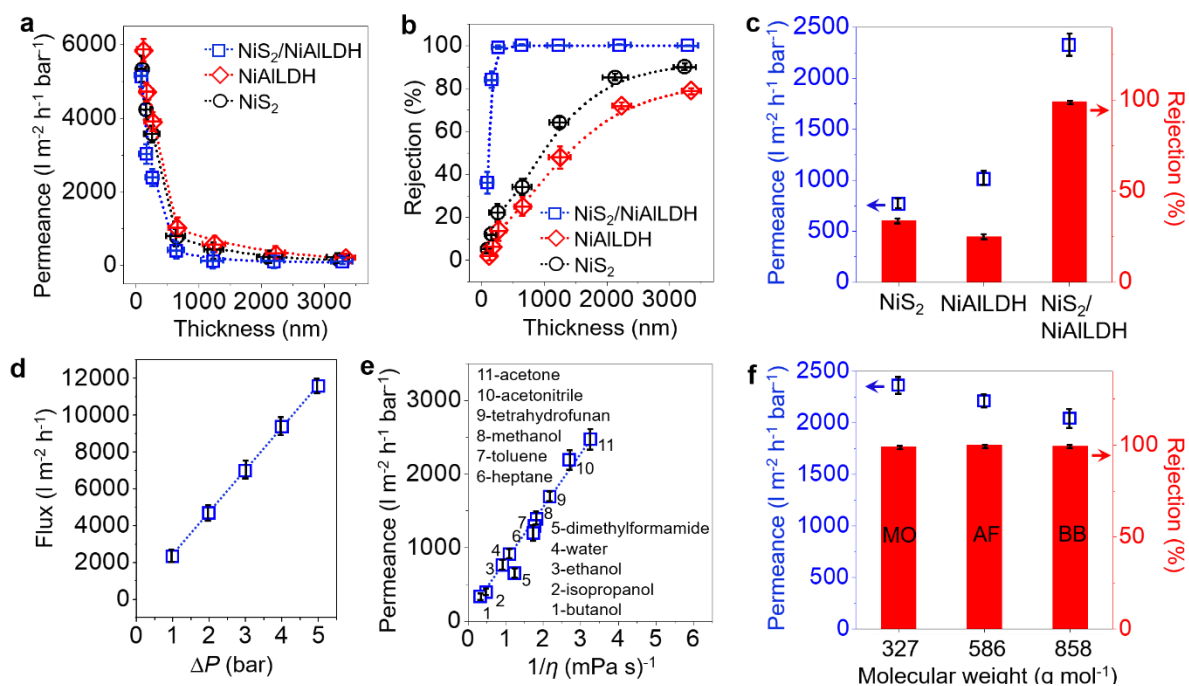


394

395 **Figure 1.** Characterizations of the TLL composite. a) TEM image of NiS₂ nanosheets
 396 heteroassembled with NiAILDH nanosheets. b) HR-TEM image showing lamellar lattice
 397 fringes with alternating contrasts, with the inset schematic depicting the stacking of the
 398 nanosheets. c) SAED indexed to be in-plane diffraction rings of TMD (T₂₀₀ and T₂₂₀) and LDH
 399 (L₁₀₀ and L₁₁₀), respectively. d) XRD patterns of pristine NiS₂ and NiAILDH, as well as
 400 NiS₂/NiAILDH composite. e) AFM image of the TLL membrane transferred from an alumina
 401 substrate to a silicon wafer. f) Height profile of the TLL membrane along the dotted line in
 402 panel (e).

403

404



405

406 **Figure 2.** Organic solvent nanofiltration (OSN). a) Acetone permeance versus thickness of
 407 selective layer. b) Rejection of methyl orange (MO) in acetone versus selective layer thickness.
 408 c) Permeance and rejection of MO in acetone through 600 ± 55 nm-thick NiS₂ and NiAILDH
 409 membranes, in comparison with 250 ± 20 nm-thick NiS₂/NiAILDH membranes. d) acetone
 410 flux through a 250 ± 20 nm-thick NiS₂/NiAILDH membrane as a function of operating pressure
 411 (ΔP); e) Permeance of pure solvents through a 250 ± 20 nm-thick NiS₂/NiAILDH membrane
 412 as a function of the inverse viscosity (η); f) permeance and rejection of various organic dyes in
 413 acetone through a 250 ± 20 nm-thick NiS₂/NiAILDH membrane; the dyes used were methyl
 414 orange (MO), acid fuchsin (AF) and brilliant blue G (BB), with the molecular weights indicated
 415 in the x-axis.

416

417

418

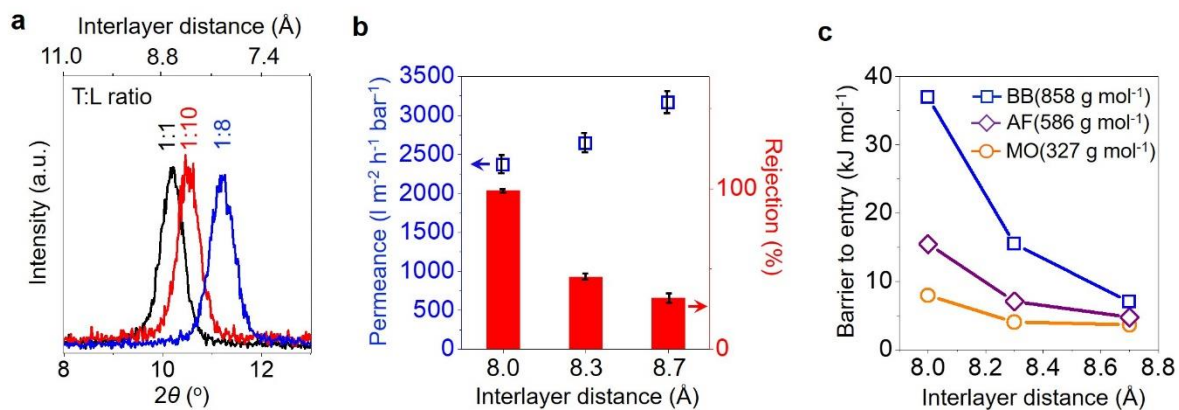
419

420

421

422

423



424

425 **Figure 3.** Effect of TMD:LDH (T:L) ratio on separation performance. a) XRD of 250 ± 20 nm-
 426 thick $\text{NiS}_2/\text{NiAlLDH}$ membranes with various T:L mass ratio. b) Permeance and rejection of
 427 MO in acetone through 250 ± 20 nm-thick $\text{NiS}_2/\text{NiAlLDH}$ membranes as a function of
 428 interlayer distance. c) Energy barrier for various organic solutes (with different molecular
 429 weights) in acetone as a function of interlayer distance for 250 ± 20 nm-thick $\text{NiS}_2/\text{NiAlLDH}$
 430 membranes.

431

432

433

434

435

436

437

438

439

440

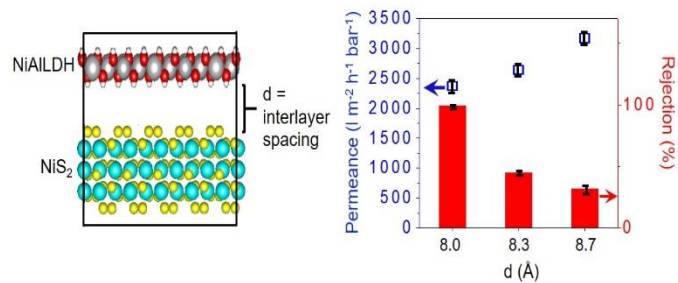
441

442

443

444

445 Two-dimensional transition-metal dichalcogenides-based membrane for ultrafast solvent
446 permeation



447

448

449

450